



PERGAMON

Available online at [www.sciencedirect.com](http://www.sciencedirect.com)

SCIENCE @ DIRECT®

Deep-Sea Research I 50 (2003) 657–680

DEEP-SEA RESEARCH  
PART I

[www.elsevier.com/locate/dsr](http://www.elsevier.com/locate/dsr)

# Ekman-induced turbulence over the continental slope in the Faeroe–Shetland Channel as inferred from spikes in current meter observations

Phil Hosegood\*, Hans van Haren

*Netherlands Institute of Sea Research (NIOZ), P.O. Box 59, 1790 AB Den Burg, The Netherlands*

Received 7 May 2002; received in revised form 15 October 2002; accepted 7 February 2003

## Abstract

Data from Aanderaa RCM-8 current meters, deployed on the continental slope of the Faeroe–Shetland Channel between depths of 471 and 1000 m, show intermittent spike-like reductions in current speed of ~20–40%. The spikes have a duration of only one data value, corresponding to the unusually short sampling period of 1 min. Associated with the spikes are concurrent deflections in the current direction records, with a mean value of 7° and in a predominantly clockwise sense. The spikes furthermore occur only when the current direction has a poleward long-slope component when the shallow water is to the right. We reject instrumental deficiency as the cause of the spikes, and find that the negative bias is caused by the cosine response of the mechanical current meter when misaligned with the mean flow. The misalignment is due to turbulence generated by instabilities in the bottom boundary layer (BBL) caused by the downslope Ekman transport of buoyancy. The veering in current direction between 8 and 47 m above the seabed and the hourly averaged current direction are consistent with such a mechanism, whilst the intermittency is explained by the bursting phenomenon in a BBL. Both the quasi-period of ~600 s and the duration of the spikes are in accordance with previous fieldwork and laboratory experiments and, in conjunction with a thickening of the boundary layer induced by the downwelling Ekman transport, explain the predominance of the spikes at heights of 34 and 47 m. Oblique internal wave reflection also plays a potential role in generating turbulence at the upper interface of the BBL higher up the slope where the stratification is comparatively strong, but the Ekman transport represents the dominant mechanism. Our findings cause concern for the reliability of data from traditional rotor- and vane-type current meters sampling at lower rates in turbulent near-bed regions where the turbulent properties of the flow will be averaged out in the sampling process, potentially causing an underreading of the true current speed.

© 2003 Elsevier Science Ltd. All rights reserved.

*Keywords:* Bottom Ekman layer; Continental slope; Downwelling; Turbulence; Intermittency; UK; Faeroe–Shetland Channel; 60°30'N 2°W–61°30'N 5°W

## 1. Introduction

The measurement of ocean currents by mechanical current meters employing a rotor and vane configuration can be problematic in environments

\*Corresponding author. Tel.: +31-222-369406; fax: +31-222-319674.

*E-mail address:* [hosegood@nioz.nl](mailto:hosegood@nioz.nl) (P. Hosegood).

subject to high-frequency perturbations. Traditionally, such instruments, to sample current speed, used Savonius rotors, which suffer from overspeeding due to their non-linear response under accelerating and decelerating flows (Fofonoff and Ercan, 1967; Saunders, 1980), and in all unsteady, non-reversing flows (Karweit, 1974). Overspeeding of vector-averaging current meters (VACMs) employing a Savonius rotor may transpire in flows with a vertical oscillatory component due to the greater response of the Savonius rotor compared to the vane under such conditions (Kalvaitis, 1974). The filtering technique effected by the vector-averaging process is rendered ineffectual by the time constant of the vane being greater than that of the rotor, and its response lagging behind that of the rotor. The majority of field studies assessing the accuracy of current meters have focused on near-surface regions affected by surface waves, either directly

by the orbital motions of the water particles on the current meter or indirectly by the vertical motion of the mooring induced by wave motion acting on mooring components. In each case, errors are reduced nearer the surface because the orbital wave motions sweep away unsteady flow generated by the along-axis motion (Saunders, 1976).

Underreading of the mean flow by a Savonius rotor will occur when a co-linear fluctuating velocity component has an amplitude greater than the mean flow, causing flow reversal (Saunders, 1980). VACMs using shielded paddle-wheel rotors, such as Aanderaa RCM-7s and RCM-8s, have been shown in field tests to suffer from a continuous underreading of current speed due to mooring vibration induced by a mean flow passing an obstruction under tension, for example, buoyancy elements in a mooring line (Loder et al., 1990; Loder and Hamilton, 1991; Hamilton et al., 1997). A rotor shielding effect is facilitated

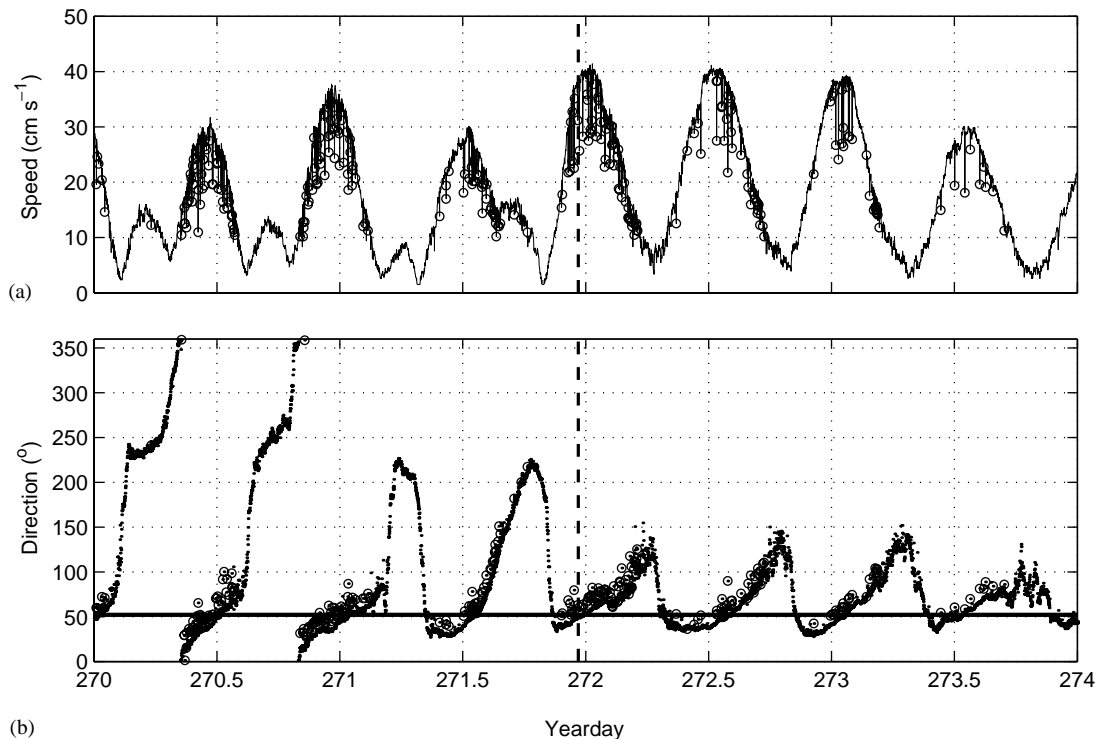


Fig. 1. (a) Current speed and (b) direction from RCM-8,  $z = 47$  at 800m depth, PROCS 99-3. Spikes are indicated as circles (as defined in Section 2.3). Horizontal line in (b) represents  $52^{\circ}\text{N}$ , corresponding to positive long-slope direction. Dashed vertical line corresponds to time of CTD cast (see Fig. 13).

by high-frequency oscillations in a direction normal to the mean flow leading to a misalignment of the VACM with the relative flow; the rotor profile exposed to the flow is thus obstructed by the shield, causing the rotor to underread the absolute current speed. Significantly, however, data from the same field study on Georges Bank (Hamilton et al., 1997) suggested that electromagnetic current meters (EMCMs) were also subject to underreading due to the mooring vibration, implying that an additional mechanism causes underreading.

The above examples of data degradation were for shallow (<150 m) water where the influence of surface waves was still present and current speeds were relatively high (>50 cm s<sup>-1</sup>). Here we present data acquired from a number of Aanderaa RCM-8s (VACMs), deployed near the seabed during a 1999 field study in the Faeroe–Shetland Channel, at depths in excess of 471 m. They show evidence of numerous short, spike-like reductions in current speed (Fig. 1) that are unlike any previously documented examples of data degradation outlined above, in a region well removed from the influence of surface waves, and typified by relatively steady flows with speeds typically <60 cm s<sup>-1</sup>. The current meters sampled at the unusually fast rate of once per minute with the purpose of resolving the strong current variability over short time scales associated with internal waves interacting with the boundary layer above a sloping bottom, the subject of the study. The RCM-8s were all equipped with unshielded Savonius rotors which, on the evidence of past research, would be expected to suffer from overspeeding as opposed to the apparent underreading, with the exception of a co-linear fluctuating component of the flow. However, the intermittent occurrence of the spikes throughout the affected records, and the tendency for the instruments at the top of the moorings to be most affected, suggests an instrumental cause alone as being insufficient to explain the presence of the spikes. We investigate here the cause of the spikes in our data from both instrumental and physical perspectives in an effort to clarify the limitations of the instruments deployed on deep-sea moorings and to assess the insight into the physical environment that may be gained.

## 2. Field study, instrumentation and data handling

### 2.1. Field study

Moorings were deployed during the physical/bio-geochemical oceanographic project processes on the continental slope (PROCS), whose primary goal is to investigate the interaction between sloping topography and internal oceanic motions. Two cruises were conducted, PROCS 99-1 and PROCS 99-3, during the periods 14 April–5 May and 21 September–13 October, respectively, in 1999. The locations of the moorings were along a transect perpendicular to the continental slope on the southern side of the Faeroe–Shetland Channel (Fig. 2), in water of depth 471–1000 m, in a region where the main thermocline is found between depths of 400 and 600 m. Considering the direction of the dominant surface flow, positive long-slope direction ( $y$ ) is to a heading of 52°N (True North), whilst the positive cross-slope direction ( $x$ ) is to a heading of 142°N. The vertical coordinate is upward from the bottom ( $z = 0$  m). Fig. 3 illustrates the location of the moorings over the slope and the instrumentation from which data are available. CTD profiles were also taken and are referred to later in relation to the bottom mixed layer height.

### 2.2. Instrumentation

Each mooring was identical in configuration, consisting of three RCM-8 and one RCM-9 Aanderaa current meters, and two Technicap PPS 4/3 sediment traps on which NIOZ (Royal Netherlands Institute for Sea Research) optical backscatter sensors and tilt meters were mounted (Fig. 4). Buoyancy was provided in-line by 20 Benthos glass spheres at 25 kg each, located at  $z = 87$  m, whilst a recovery beacon marked the top of the mooring at  $z = 100$  m. Data from the NIOZ-designed tilt meter at  $z = 30$  m are considered here as an indication of the mooring motion that may affect the performance of the current meters. Data output is in the form of two angles in orthogonal directions,  $X$  and  $Y$ , sampled instantaneously every 4 min. Total tilt ( $T_i$ ) is calculated

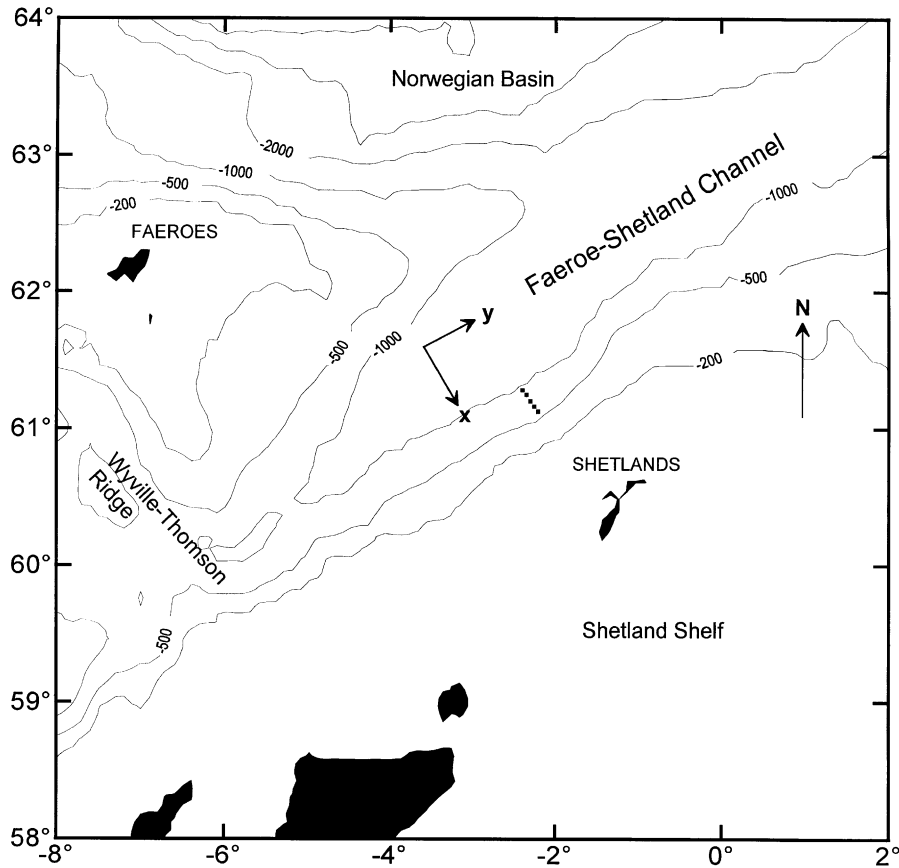


Fig. 2. Map of study region indicating positions of moorings (squares).

as follows:

$$T_i = \cos^{-1}((\cos Y)(\cos Z)), \quad (1)$$

where

$$Z = \sin^{-1} \left[ \frac{(\sin X)(\cos Y)}{(1 - ((\sin X)(\sin Y))^2)^{1/2}} \right]. \quad (2)$$

RCM-8s and RCM-9s differ in their sampling strategy; the former are mechanical VACMs, vector averaging 12s samples of current speed sensed by a Savonius rotor and direction over the recording interval, which during PROCS was 1-min such that five samples were averaged per data point. The RCM-9 is a Doppler current sensor, vector averaging horizontal currents measured by

each acoustic ping in an area of 0.5–2 m from the instrument. Six hundred pings are averaged over the recording interval, also set to 1 min.

### 2.3. Definition of spikes in speed record

The focus of this paper is the spikes observed in our data, seen as isolated drops in current speed, and are defined as those points where

1. The first difference of speed is in excess of a threshold equivalent to a threefold multiple of its standard deviation when calculated within a subjectively defined range ( $\pm 0.05 \text{ cm s}^{-2}$ ) which excludes spikes that would otherwise bias the calculation of the standard deviation.

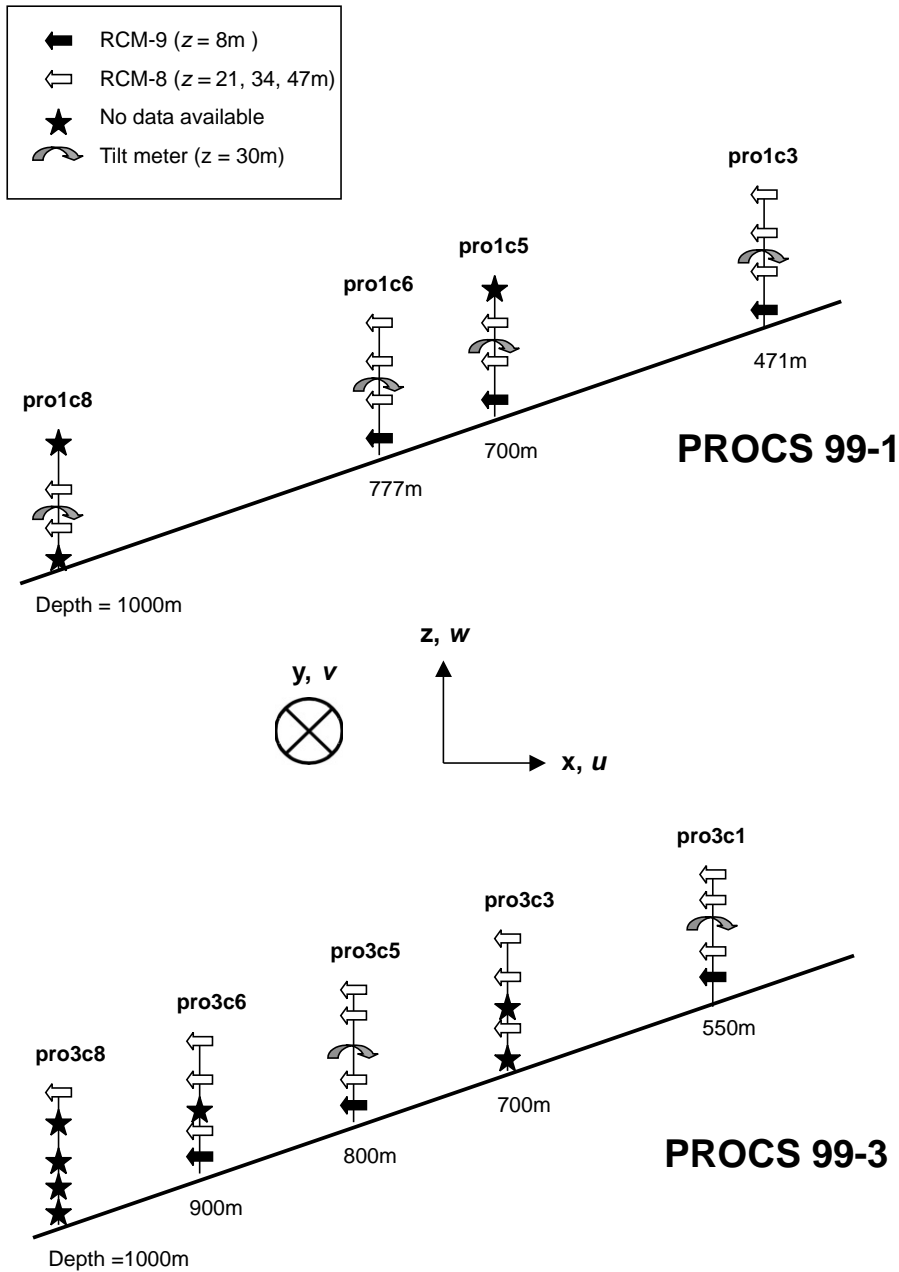


Fig. 3. Location of moorings over continental slope and coordinate axes.

2. The current speed is in excess of  $10 \text{ cm s}^{-1}$ , required to eliminate inaccuracies inherent to the instrument at low current speeds.

From the current direction (Fig. 1b) it may be seen that associated with each spike in the speed

record is a small deviation in direction away from the 'hourly averaged' current direction. For want of a better term, we use the term 'hourly averaged' current to define the current speed and direction on an approximately hourly time scale, thereby excluding the influence of the spikes whose time

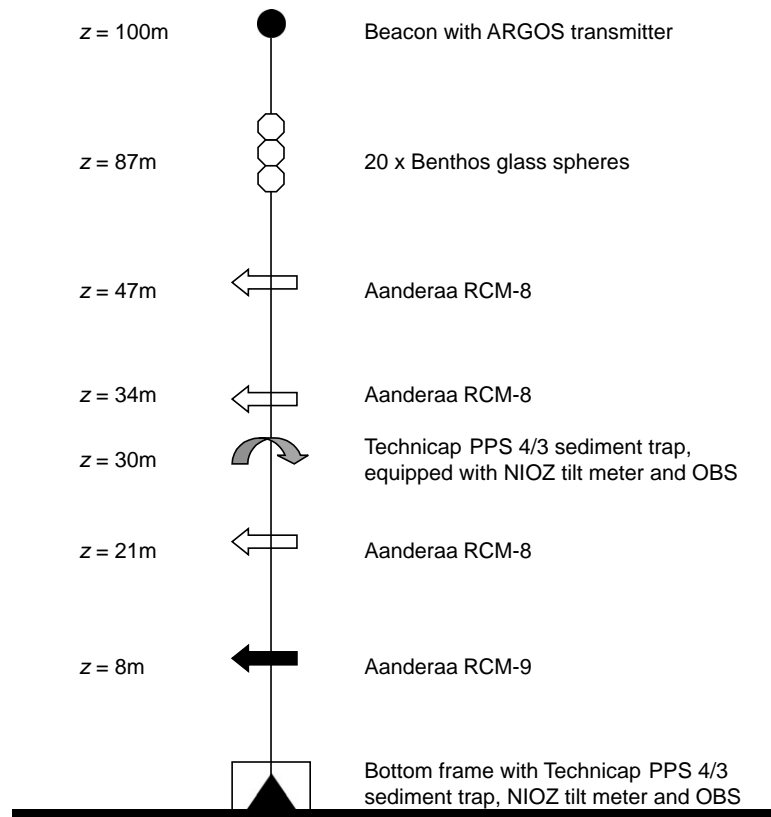


Fig. 4. Mooring configuration (OBS = optical backscatter sensor).

scale is  $O(1 \text{ min})$ , but being of a scale less than the tidal frequencies. Thus, the term in this case does not imply that actual averaging is carried out. Having defined those points that constitute a spike, we further categorise those records subject to spikes. Although this is a subjective procedure, both from the perspective of what constitutes a spike and which records are affected, it is done so here for the purposes of the analysis in this paper. Thus, no consideration is given to the processes or mechanisms that may be responsible for the spikes in stating which records are affected.

Spiked records are arbitrarily defined as records which exhibit spikes whose mean percentage drop in speed exceeds 20% and mean change in direction exceeds  $3^\circ$  (cf. Section 3.4). The eight records that satisfy these requirements are highlighted in Table 1. An essential point to stress here is that records other than those defined here as spiked do still show spikes of the same nature, but

the low number/or lesser size of the spikes complicates the analysis without aiding their interpretation.

### 3. Results

#### 3.1. General current variability with water depth

The current regime is not significantly different between moorings other than at a depth of 550 m, where currents are more energetic than at greater depths over the slope. As opposed to the solely negative bias observed in the high-frequency components of the long-slope flow (Fig. 5a), notably at 1000 m, the cross-slope current components (Fig. 5b) exhibit both positive and negative high-frequency fluctuations. The uppermost mooring at 550 m is located in a region of strong temperature gradients (Fig. 5c), active over short

Table 1  
Summary statistics from all instruments that provided good data

Mooring and depth	<i>z</i> (m)	Max. speed (cm s <sup>-1</sup> )	Threshold value (cm s <sup>-2</sup> )	% of record spiked	Mean % drop	Mean Δ <i>D</i> (°)	Mean Δ <i>D</i> of spikes (°)	% of spikes 25° < <i>D</i> < 125°
PRO1c3, 471 m	47	62.66	-0.04	2.11	-12.43	0.0006	2.35	83.29
	34	67.47	-0.07	1.86	-15.01	-0.0017	-0.54	85.24
	21	59.51	-0.05	2.76	-11.35	-0.0004	-0.09	82.96
	8	63.56	-0.08	2.94	-19.91	0.001	-2.13	90.09
PRO1c5, 700 m	<b>34</b>	<b>66.60</b>	<b>-0.04</b>	<b>3.58</b>	<b>-23.86</b>	<b>0.0127</b>	<b>12.08</b>	<b>91.71</b>
	<b>21</b>	<b>63.97</b>	<b>-0.04</b>	<b>3.66</b>	<b>-30.46</b>	<b>0.0122</b>	<b>3.92</b>	<b>84.71</b>
	8	68.45	-0.07	1.87	-18.45	0.0098	-0.71	71.94
PRO1c6, 777 m	<b>47</b>	<b>73.95</b>	<b>-0.04</b>	<b>1.67</b>	<b>-22.26</b>	<b>0.0128</b>	<b>5.71</b>	<b>85.95</b>
	34	75.79	-0.04	1.23	-13.06	0.0155	3.09	82.2
	24	74.21	-0.04	1.81	-13.83	0.0102	2.49	83.9
PRO1c8, 1000 m	8	70.89	-0.07	1.71	-17.18	0.0100	-1.76	75.81
	<b>34</b>	<b>65.55</b>	<b>-0.04</b>	<b>1.89</b>	<b>-27.90</b>	<b>-0.0008</b>	<b>3.45</b>	<b>64.69</b>
	21	65.02	-0.05	1.33	-11.50	-0.000	-1.07	27.97
PRO3c1, 550 m	<b>47</b>	<b>60.64</b>	<b>-0.04</b>	<b>3.09</b>	<b>-34.41</b>	<b>-0.0035</b>	<b>23.87</b>	<b>78.49</b>
	<b>34</b>	<b>61.61</b>	<b>-0.05</b>	<b>8.34</b>	<b>-44.64</b>	<b>-0.0038</b>	<b>7.51</b>	<b>73.59</b>
	21	62.66	-0.04	1.37	-17.02	-0.0040	-5.10	57.20
	8	72.36	-0.07	1.78	-19.59	-0.0007	-0.49	75.57
PRO3c3, 700 m	47	51.11	-0.02	0.80	-14.04	0.0044	0.94	36.08
	34	58.74	-0.03	1.19	-18.28	0.0035	5.51	48.29
	21	52.95	-0.03	0.95	-10.79	0.0041	-2.27	17.02
PRO3c5, 800 m	<b>47</b>	<b>41.40</b>	<b>-0.03</b>	<b>1.87</b>	<b>-26.46</b>	<b>-0.0087</b>	<b>14.02</b>	<b>95.95</b>
	34	42.19	-0.03	0.71	-10.04	-0.0088	1.85	87.23
	21	40.61	-0.03	0.97	-12.53	-0.0084	0.36	91.10
	8	42.53	-0.07	0.40	-21.71	-0.0069	-0.73	98.73
PRO3c6, 900 m	47	49.80	-0.03	0.93	-16.60	-0.0090	6.24	87.50
	34	51.64	-0.03	0.85	-11.79	-0.0088	0.30	81.55
	21	49.01	-0.04	0.90	-11.45	-0.0094	-1.58	80.90
	8	56.22	-0.07	1.23	-20.10	-0.0085	-1.28	81.48
PRO3c8, 1000 m	<b>47</b>	<b>47.70</b>	<b>-0.04</b>	<b>4.2</b>	<b>-39.98</b>	<b>-0.0095</b>	<b>4.89</b>	<b>95.67</b>

Spiked records in bold italic. Δ*D*=change in the direction between adjacent points.

time scales at a depth where the stratification and slope angle are favourable for the generation of the semidiurnal internal tide. Spectra of kinetic energy at *z* = 47 m for all moorings during PROCS 99-3 (Fig. 6) confirm the higher energy levels at 550 m for all frequencies, σ, except at the semi-diurnal tidal frequency, at which all depths exhibit similar values. For σ > 2 cpd (1 cpd = 2π/86400 s<sup>-1</sup>), kinetic energy decreases with depth to 800 m, attributable in part to the influence of internal waves higher up the slope; below 800 m, the spectra are quantitatively similar except at higher frequencies; at 1000 m the spectral slope decreases for σ > 30 cpd, possibly attributable to the presence of spikes in this record. The same decrease in

slope is also evident for 800 m but to a lesser extent.

The internal wave band, defined as *f* < σ < *N*, where *f* is the Coriolis parameter and

$$N = \left( \frac{-g \Delta\rho}{\rho_0 \Delta z} \right)^{1/2} \tag{3}$$

is the buoyancy frequency, calculated from CTD data for 100 < *z* < 150 m, is substantially reduced below 550 m. At 550 m, *N* ≈ 45 cpd, giving a minimum free internal wave period of ~32 min, whilst at 1000 m, *N* ≈ 7 cpd corresponding to a period of ~200 min. This will be seen later to have implications for the potential of internal waves in facilitating the occurrence of the spikes.

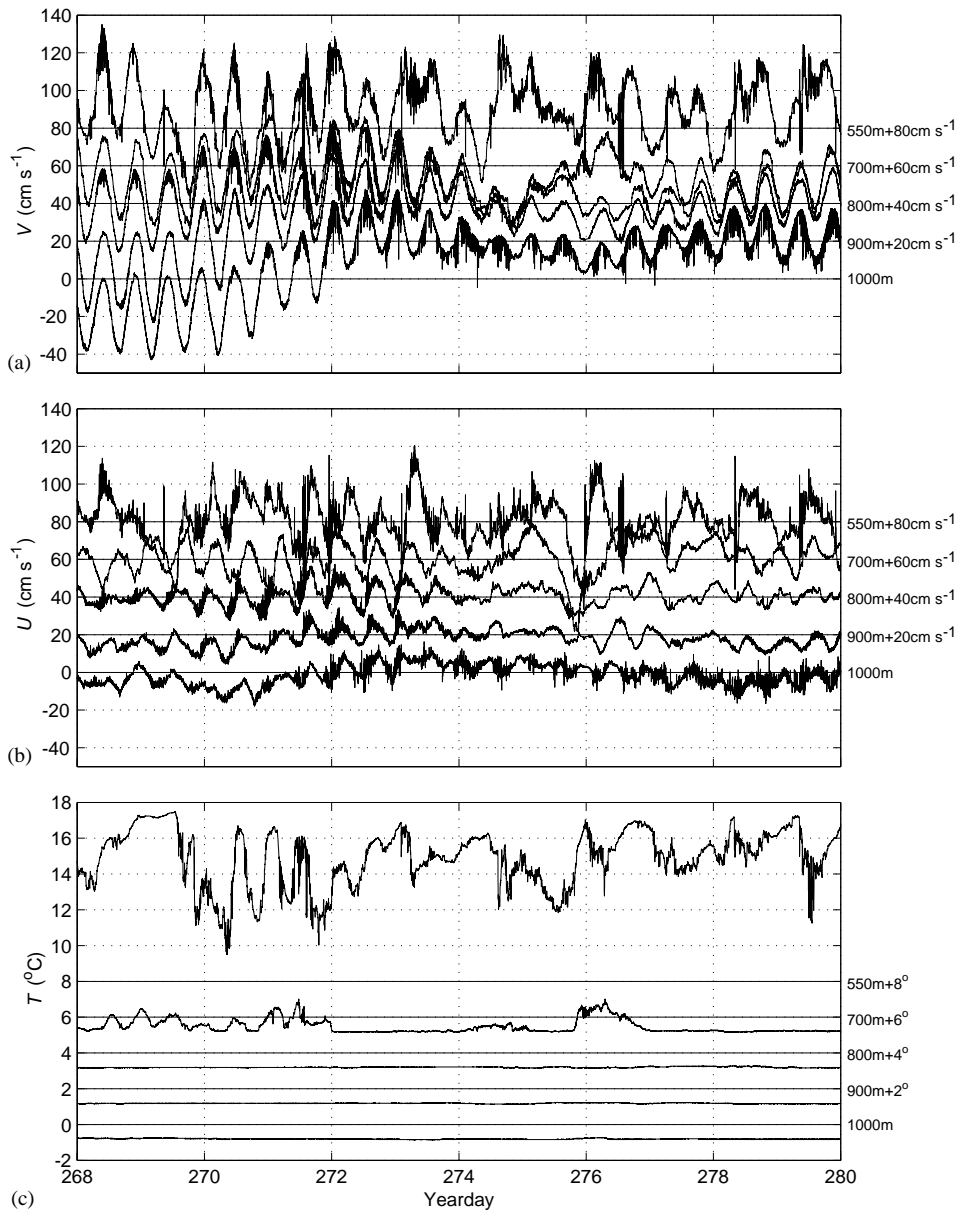


Fig. 5. (a) Long-slope velocity, (b) cross-slope velocity, (c) temperature, at  $z = 47$  m, all moorings, PROCS 99-3. Note all records above 1000 m are offset by  $20 \text{ cm s}^{-1}$  and  $2^\circ \text{C}$ , and multiples thereof.

### 3.2. Current variability with height above seabed

Differences exist between instruments deployed on the same moorings. Smoothed spectra of kinetic energy for all instruments at 800 m depth

during PROCS 99-3 demonstrate the higher noise levels exhibited by the RCM-9 (Fig. 7), whilst higher noise levels are attributed to spikes in the RCM-8 record from  $z = 47$  m. At the Nyquist frequency ( $\sigma_{\text{Nyquist}} = 720 \text{ cpd}$ ) kinetic energy at

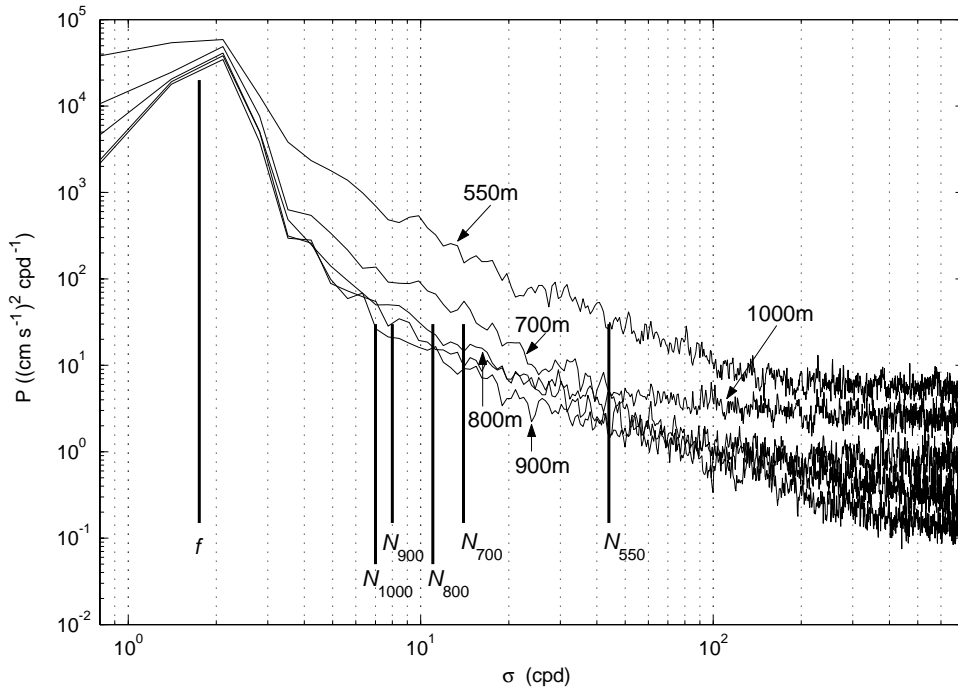


Fig. 6. Moderately smoothed spectra of kinetic energy (degrees of freedom (df)=36) from RCM-8s at  $z = 47$ , all moorings, PROCS 99-3.  $N_{\text{depth}}$  = buoyancy frequency (cf. Section 3.1) at each mooring (subscript refers to approximate depth for which  $N$  is calculated).

$z = 8$  and  $47$  m is comparable (Fig. 7), but in the absence of spikes, kinetic energy levels at  $\sigma_{\text{Nyquist}}$  at  $z = 8$  m (RCM-9) are approximately 1–2 decades higher than those of the RCM-8s at  $z = 21$  and  $34$  m. The slope of kinetic energy spectrum decreases at  $\sigma \sim 30\text{--}40$  cpd for the RCM-9, whereas the decrease in slope attributed to the spikes begins at  $\sigma \sim 100$  cpd.

It is clear from Table 1 that none of the RCM-9s at  $z = 8$  m are classified as ‘spiked’; this may be a reflection of the criteria for defining spikes, as the higher noise levels of the RCM-9s result in a higher standard deviation of current speed, thus requiring substantially larger drops in speed to indicate a spike. However, when the accelerations experienced by the RCM-8s are compared with those of the RCM-9s, it is clear that periods of enhanced accelerations occur concurrently for both instruments, although to a lesser extent for the acoustic instrument (Fig. 8). The enhanced noise, or spikes, furthermore appears to occur in packets with a period corresponding to that of the

semi-diurnal tidal frequency. It thus appears that the mechanism facilitating the occurrence of spikes in the RCM-8 records is also experienced by the RCM-9s but to a lesser extent, or that the effect is lessened by the spatial averaging the RCM-9 employed in its sampling method.

### 3.3. Mooring motion

The performance of RCM-8s is compromised beyond  $12^\circ$  inclinations of the instrument. Short period inclinations of lesser magnitude may also reflect rapid mooring motion, leading to the degradation of the performance of mechanical current meters in particular (Hamilton et al., 1997). Beyond  $12^\circ$  erroneous data will be returned; the gimbals on the mounting permit a tilt of  $26^\circ$  before the instrument itself starts to tilt, giving a total tilt required of  $38^\circ$  before errors result. Table 2 summarises the maximum tilts observed by each sediment trap at  $z = 30$  m, from which it may be seen that none of the tilt meters

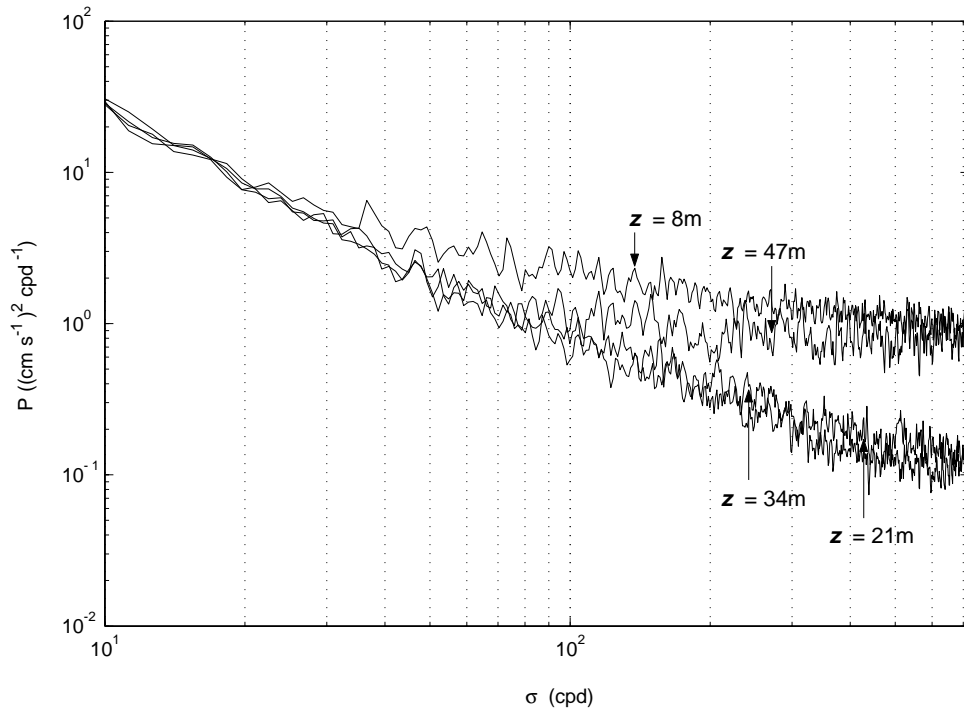


Fig. 7. Smoothed spectra ( $df=73$ ) of kinetic energy, all instruments, at 800 m depth, PROCS 99-3. Note higher noise levels exhibited by RCM-9 at  $z = 8$  for  $\sigma > 40$  cpd, and the enhanced noise at  $z = 47$  (RCM-8) for  $\sigma > 90$  cpd.

experienced inclinations in excess of the critical value of  $38^\circ$ .

By sub-sampling the current speed at once per 4 min, a linear relationship between the squared amplitude of the horizontal current and tilt  $X$  is found. This is expected for the drag of the mooring under the influence of the hourly averaged flow, assuming that the tilt meter aligns itself with the flow direction. This expectation is based on the instantaneous static balance of the sediment trap between the drag force,  $F_d$ , acting on the mooring and its weight,  $F_w$ :

$$F_w \tan X = F_d = CU^2, \quad (4)$$

where  $C$  contains the cross-sectional area exposed normal to the current and the drag coefficients, and  $U$  is the current amplitude (van Haren, 1996). As tilt  $Y$  is orthogonal to tilt  $X$ , the former represents motion in the direction normal to the 'mean' flow.

Tilt  $Y$  exhibits a high-frequency oscillatory component whose amplitude is modulated in 'packets' which occur with a semi-diurnal period (Fig. 9). By high-pass filtering (cut-off frequency  $\sigma = 24$  cpd) the two time series, the 'packets' of high-frequency components are also seen in the tilt  $X$  data. This suggests the instrument to be subject to rapid perturbations in all directions, although to a larger extent in the direction normal to the flow.

### 3.4. Relation between spikes and current direction

The occurrence of spikes in the current speed is related to the current direction in three ways:

1. Spikes occur predominantly when the current direction is within an approximate range of headings, between  $25^\circ\text{N}$  and  $125^\circ\text{N}$ .

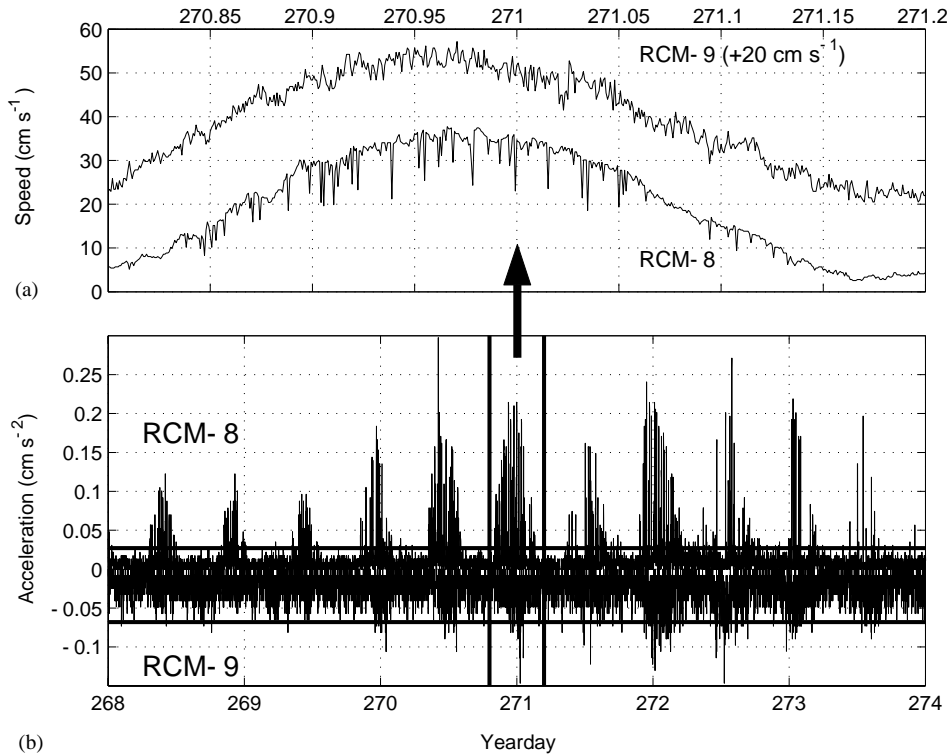


Fig. 8. (a) Detailed speed records from RCM-8 and RCM-9 and (b) absolute values of acceleration from RCM-8 at  $z = 47$  and RCM-9 (negative values) at  $z = 8$ , at 800 m depth, PROCS 99-3. Solid horizontal lines represent the respective thresholds for defining a spike; RCM-8 =  $0.027 \text{ cm s}^{-2}$ ; RCM-9 =  $0.068 \text{ cm s}^{-2}$ .

Table 2  
Maximum tilts recorded at  $z = 30$  m for those instruments returning good data

Mooring and depth	Max tilt $X$ ( $^\circ$ )	Max tilt $Y$ ( $^\circ$ )	Max total tilt ( $T_i$ ) ( $^\circ$ )
PRO1c3, 417 m	18.25	5.58	18.56
PRO1c5, 700 m	21.26	5.00	21.40
PRO1c8, 1000 m	16.96	2.38	17.07
PRO3c1, 550 m	13.49	4.48	13.51
PRO3c5, 800 m	10.39	2.01	10.43

- As current speed increases, the heading of the current at the time of spikes tends to  $52^\circ$ , corresponding to a poleward long-slope flow.
- Associated with the spikes in the speed records are concurrent clockwise/up-slope deflections in the direction records.

The first two observations are related in that the spikes exist only in those parts of the records where the current tends towards a positive long-slope direction, and that this tendency increases with current speed (Fig. 10). The average heading of the spike with the maximum current speed of each of the eight spiked records is  $58^\circ$ . For PROCS 99-1, 84% of the spikes occur within the range of headings  $25\text{--}125^\circ$ , with the proportion dropping to 82% during PROCS 99-3 (due mainly to the record at 550 m), whilst 91% of the spikes in all spiked records have a positive long-slope component. The best illustration of the dependence of the spikes on current direction is the RCM-8 from 1000 m during PROCS 99-3 (Fig. 11). Unfortunately, the loss of all other instruments on this mooring prohibits a full analysis of this mooring.

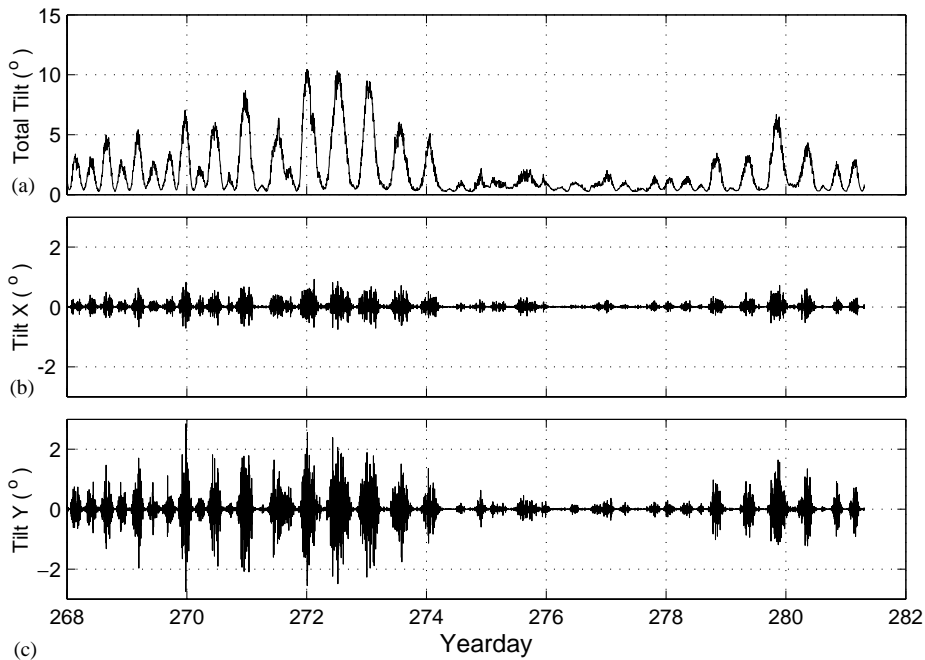


Fig. 9. Tilt meter data from  $z = 30$  at 800 m depth, PROCS 99-3: (a) total tilt and (b, c) high-pass filtered tilt  $X$  and  $Y$  components, respectively; cut-off frequency,  $\sigma = 24$  cpd.

The deflections in current direction associated with the spikes are evident in Fig. 12. The mean change in direction between data values is, for all records, of  $O(10^{-4}–10^{-2}^\circ)$ , whilst the spikes exhibit a mean deflection of  $7^\circ$ , with 70% of those in a clockwise sense. The largest number of spikes occurs in the sector  $12.5–15^\circ$  clockwise for all spiked records except at 700 m,  $z = 21$  m, and 1000 m,  $z = 34$  m, PROCS 99-1. The record at 550 m,  $z = 34$  m, is anomalous in that it also shows deflections in the anticlockwise sense with magnitude and number comparable to those in the clockwise sense. The strong variability at this location inferred from the variance in the temperature signal (Fig. 5c) is the differentiating factor between this and lower depths, and implies the current regime as determining the orientation of the deflections, rather than the spikes themselves having an inherently clockwise deflection. Three of the four records from PROCS 99-1 show a number of spikes as occurring in the sector  $0–2.5^\circ$  anticlockwise, in particular at 700 m,  $z = 21$  m, but more significantly all records show

a comparative lack of spikes in the range  $0–7.5^\circ$  clockwise. We do not presently understand why this should be. The spiked records during both PROCS 99-1 and 99-3 at a depth of 1000 m (Figs. 12d and h) have a number of spikes showing anticlockwise deflections during periods when the direction of the mean flow is approximately constant; at this depth, the bottom slope is comparatively reduced, suggesting the slope as influencing the sense of the deflection.

### 3.5. Near-bottom mixed layer height

CTD casts taken at stations along a transect perpendicular to the slope provide information on the height,  $d$ , of the bottom boundary layer (BBL). Using the formulation of Weatherly and Martin (1978) which when applies to a flat bottom, we expect for  $3 < N_0 < 80$  cpd values of  $\sim 4.5 < d < 21.7$  m, where  $N_0$  is the buoyancy frequency in the interior outside the BBL taken as  $100 < z < 150$  m.  $\sigma_\theta$  profiles indicate that the height of the observed BBL extends to  $d_0 > 50$  m,

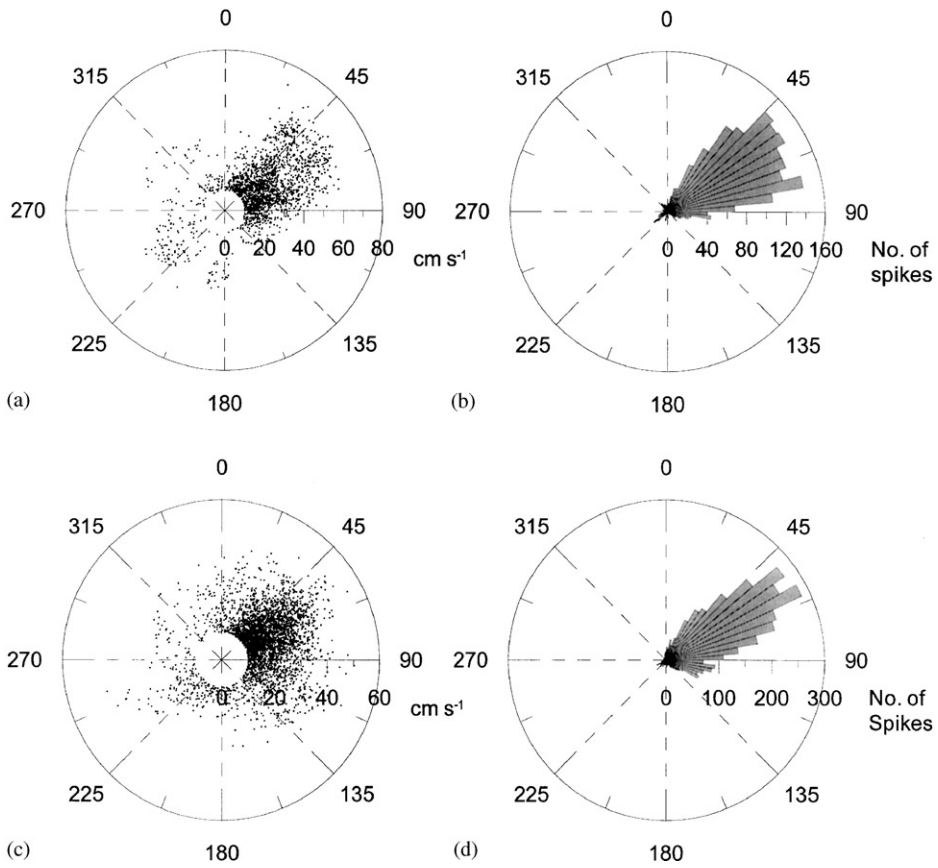


Fig. 10. Scatter plots of (a, c) current speed of spikes and their corresponding headings, and rose plots (b, d) indicating density of spikes occurring within each 5° sector for all spiked records (Section 2.3), PROCS 99-1(a, b) and PROCS 99-3 (c, d).

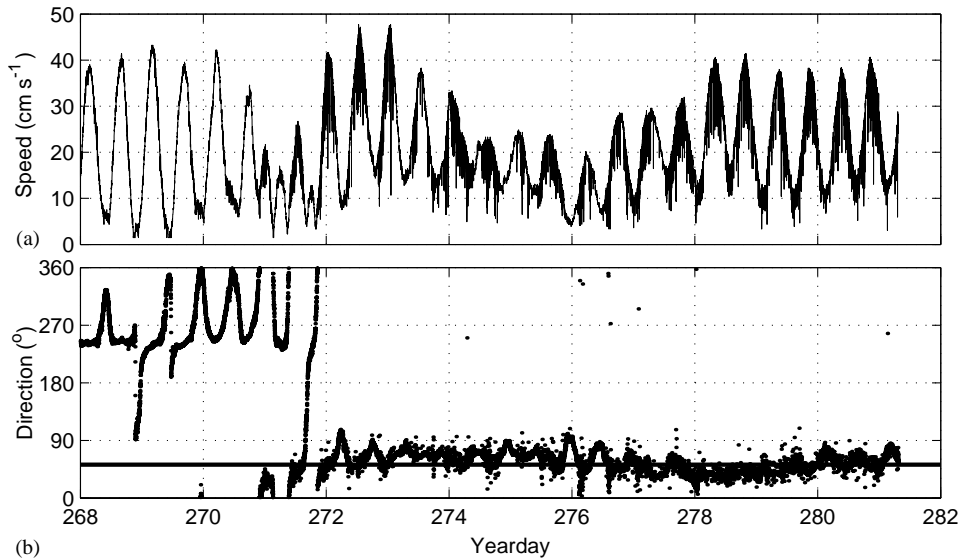
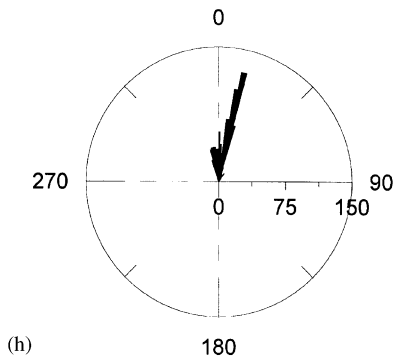
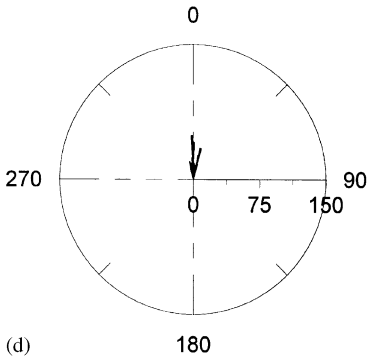
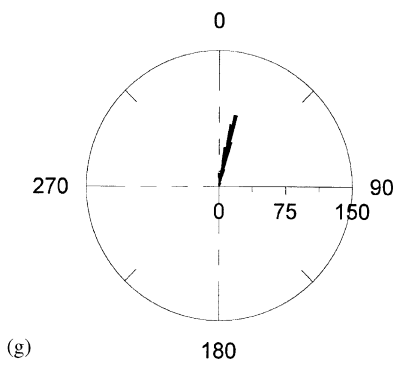
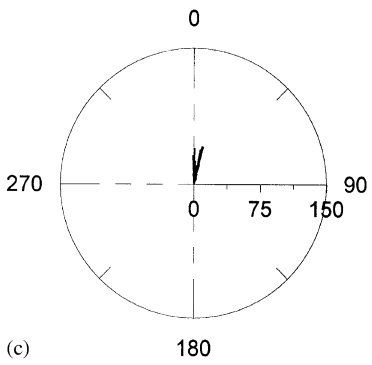
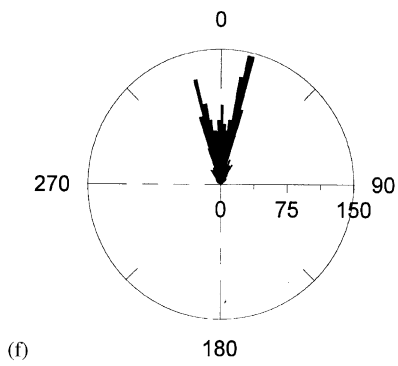
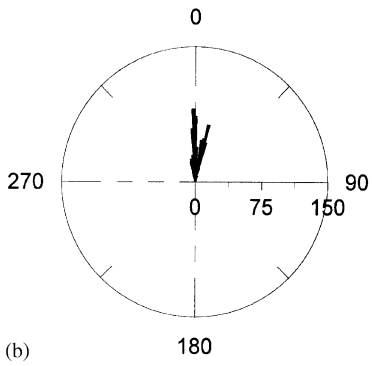
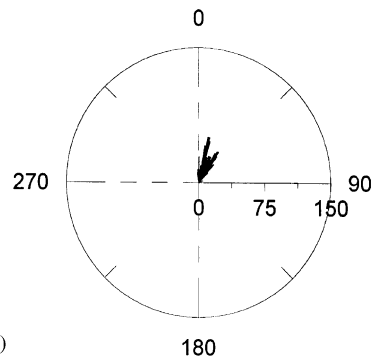
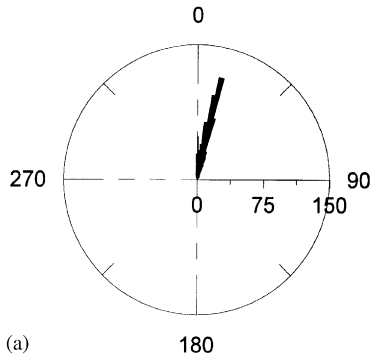


Fig. 11. (a) Current speed and (b) direction from RCM-8,  $z = 47$ , 1000 m depth, PROCS 99-3. Horizontal line in (b) is equal to 52°.



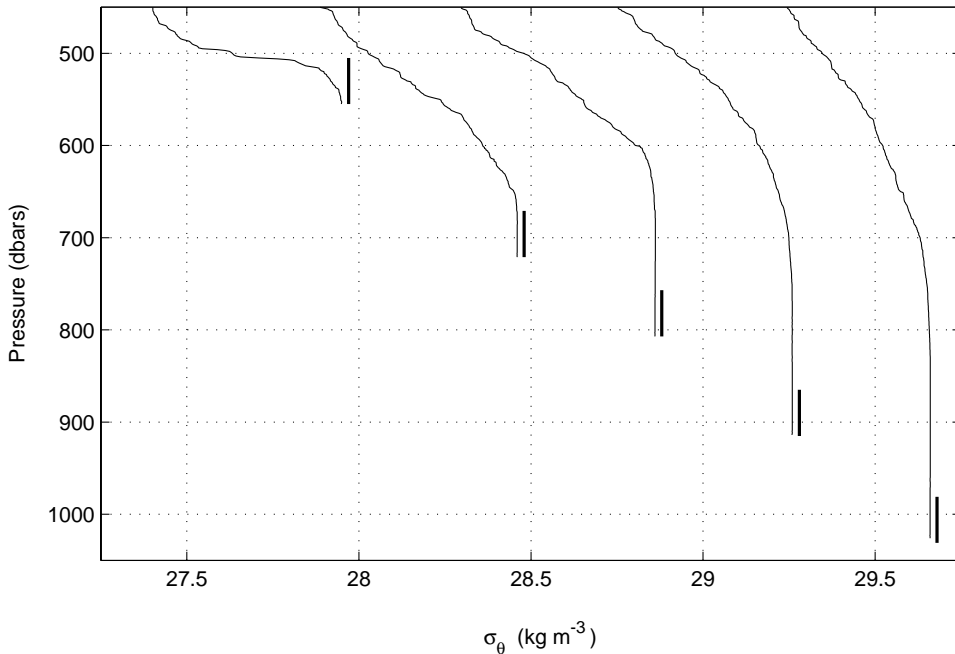


Fig. 13.  $\sigma_\theta$  profiles at stations along transect perpendicular to the slope corresponding approximately to the locations of the moorings during PROCS 99-3. Vertical lines next to each profile represent the 50 m immediately above the bottom as determined by echosounder. Each profile is offset by  $0.4 \text{ kg m}^{-3}$  from previous depth. Note the profile at 800 m was taken at the time represented by the dashed line in Fig. 1.

however (Fig. 13), and so we consider the influence of the slope on increasing  $d$ .

Trowbridge and Lentz (1991) determine  $d$  over a sloping bottom, inclined at an angle  $\alpha$  to the horizontal, where a downslope Ekman transport of light water within the BBL leads to an increase in  $d$ . A ‘slippery’ bottom boundary compared to that predicted by Ekman theory is created as the long-slope component of bottom stress and the cross-slope Ekman flux decrease (MacCready and Rhines, 1993). A steady-state limit is then attained at a time  $\tau_0 = f/(N\alpha)^2$ , where  $f$  is the Coriolis parameter, as the bottom velocity, along-isobath bottom stress and Ekman flux reach zero, halting the further evolution of the boundary layer. The time scale,  $\tau_0$ , should be increased by a factor of  $2d/\delta$ , where  $\delta$  is the natural Ekman thickness, to

account for the dilution of the buoyancy forcing by the mixing (Garrett et al., 1993). We do not include this factor however because of our lack of accurate and coincident measurements of  $d$  and the negligible difference, this ultimately makes to our results. The steady state is defined as the time when the bottom velocity, given by

$$v_b = v_i - \frac{\alpha N^2 d}{f}, \tag{5}$$

reaches zero, where  $v_i$  is the long-slope interior velocity (positive values representing downwelling favourable flow). The limiting height of the BBL under such conditions is thus given as

$$d = \frac{f v_i}{\alpha N^2} = \frac{\sqrt{2} v_i}{\gamma N}, \tag{6}$$

Fig. 12. Deflections in current direction associated with spikes in speed records, expressed as density of spikes (radial axis) per  $2.5^\circ$  sector. PROCS 99-1:  $a = 700 \text{ m}, z = 34 \text{ m}; b = 700 \text{ m}, z = 21 \text{ m}; c = 777 \text{ m}, z = 47 \text{ m}; d = 1000 \text{ m}, z = 34 \text{ m}$ . PROCS 99-3:  $e = 550 \text{ m}, z = 47 \text{ m}; f = 550 \text{ m}, z = 34 \text{ m}; g = 800 \text{ m}, z = 47 \text{ m}; h = 1000 \text{ m}, z = 47 \text{ m}$ .

where

$$\gamma = \sqrt{2} \frac{\alpha N}{f} \quad (7)$$

is a dimensionless parameter to be regarded as a measure of the influence of the bottom slope. The slope,  $\alpha$ , over the Shetland side of the channel  $\approx 0.0275 \pm 0.017$  rad ( $1.58 \pm 1^\circ$ ), which applied to (6) gives a minimum value of  $d$  of 8.3 m with a slope of 0.045 and the strongest stratification,  $N = 80$  cpd. Decreasing stratification permits the growth of the BBL to  $z = O(100$  m), whilst the steepening of the slope acts to suppress its growth (Fig. 14). For the mean value of the slope ( $\alpha = 0.0275$  rad) the steady state defined above is reached in  $\sim 80$  min for  $N = 80$  cpd, but  $\sim 50$  days for  $N = 3$  cpd. Thus, the mechanism driving a thickening of the BBL through cross-isobath Ekman transport is unlikely to reach a steady-state limit within the predominantly semidiurnal

time scales observed in our data, with the exception of the strongly stratified regions around 550 m. We thus expect a thickening of the BBL due to the influence of the slope but to a lesser extent than that predicted by (6).

#### 4. Discussion

On initial inspection, the spikes in our data appear to be physically unrealistic, which is due to instrumental error. Our observations demonstrate this not to be the case however, and we elaborate on, and discount, instrumental mechanisms facilitating underreading by VACMs, before discussing physical processes that, indirectly, can lead to the response of the current meters presented here. We distinguish between instrumental causes and those attributed to physical processes; the former are due solely to the equipment employed, and in no

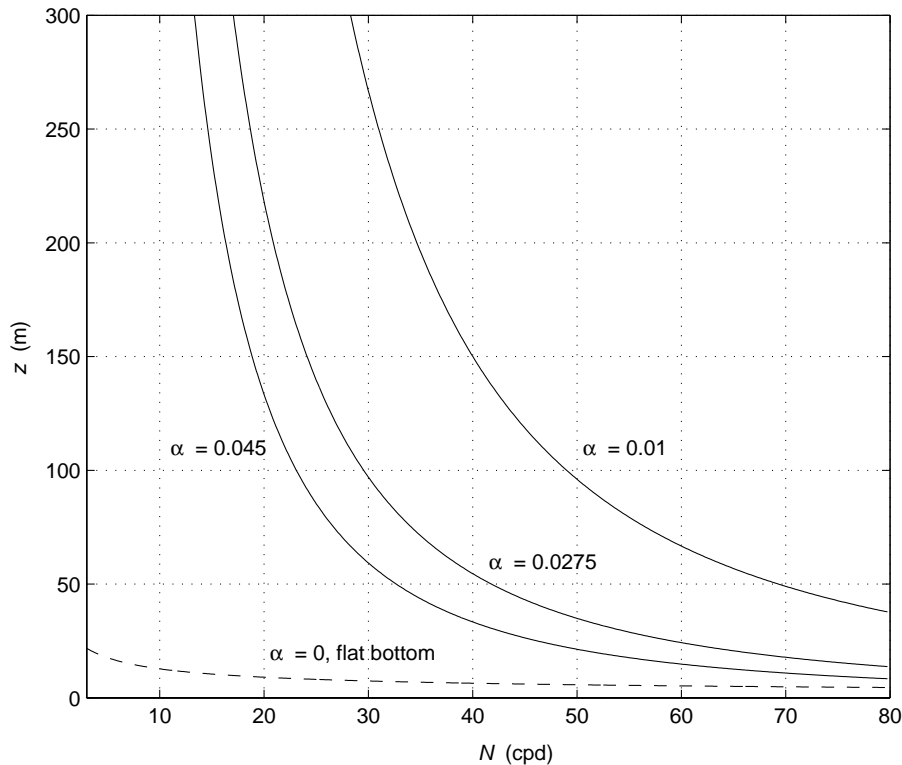


Fig. 14. Predicted height of BBL from Trowbridge and Lentz (1991)(Section 3.5), with varying  $N$  and for different slope angles,  $\alpha$  (rad). Dashed line for  $\alpha = 0$  corresponds to flat bottom formulation of Weatherly and Martin (1978).

way reflects the influence of the current regime other than a mean flow. In contrast, by physical processes we mean a specific aspect of the current regime, other than the mean flow, which forces the instrumental response, whether accurately sampled or not. Thus, the sampling error is removed in the absence of this particular property of the current. Firstly, we propose a simple routine for eliminating the spikes in the current speed records.

#### 4.1. Elimination of spikes

The spikes we observe represent, almost exclusively, only a single data value of 1 min, and as such they are easily filtered out by substituting the value of the spike with the preceding value. In the rare event that the spike spans more than 1 min, the second erroneous point is replaced by a linear interpolation between the points either side (Fig. 15). Thus, only those points representing spikes are altered in contrast to a running median filter that alters the entire time series or a low pass filter (cut-off  $\sigma \sim 96$  cpd), which eliminates the spikes but at the expense of significant reductions in current speed. Surprisingly, the spectra for the raw and the cleaned data are almost identical (Fig. 15b), suggesting that the high-frequency portion is not solely attributable to the spikes, and that the records are noisier on the whole even following the removal of the spikes.

#### 4.2. Rejection of instrumental error

Because of the vector-averaging method employed by the RCM-8, the spikes may represent missed or erroneous samples, returning a zero for one or more of the samples, during the sampling period. If this were the case one would expect drops in current speed of 20% and multiples thereof. Whilst for some of the records the *mean* percentage drop exhibited by the spikes (Table 1) is  $\sim 20\%$ , the scatter of values for the percentage drop in current speed represented by the spikes illustrates that no tendency exists (Fig. 16). Furthermore, if instrumental malfunction were responsible for the return of zero values during a recording interval, the spikes would be evident for sustained periods, irrespective of the prevalent current characteristics, and not on so many instruments (A. Bjervamoen, Aanderaa Instruments, personal communication).

Field studies in shallow water on Georges Bank found mooring vibration to cause rate under-reading by RCM-8s equipped with shielded paddle-wheel rotors and by EMCs, as compared to ship-mounted ADCP measurements (Loder et al., 1990; Loder and Hamilton, 1991; Hamilton et al., 1997). Whilst during PROCS unshielded Savonius rotors were used, the underreading by EMCs forces us to consider a mechanism other than rotor shielding as causing the spikes, in particular given the apparent perturbations to the

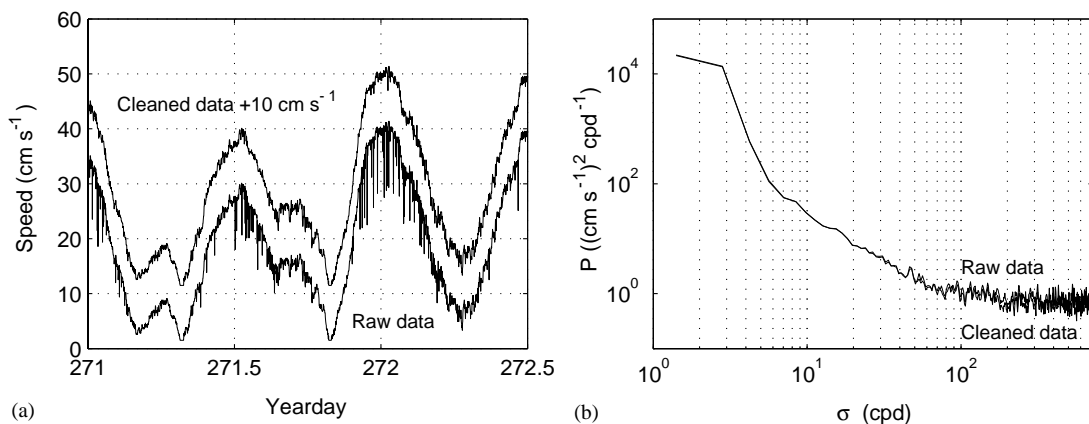


Fig. 15. (a) Current speeds and (b) kinetic energy ( $df = 73$ ) for cleaned data (following filtering as described in Section 4) and raw data from  $z = 47$  (RCM-8), 800 m depth, PROCS 99-3.

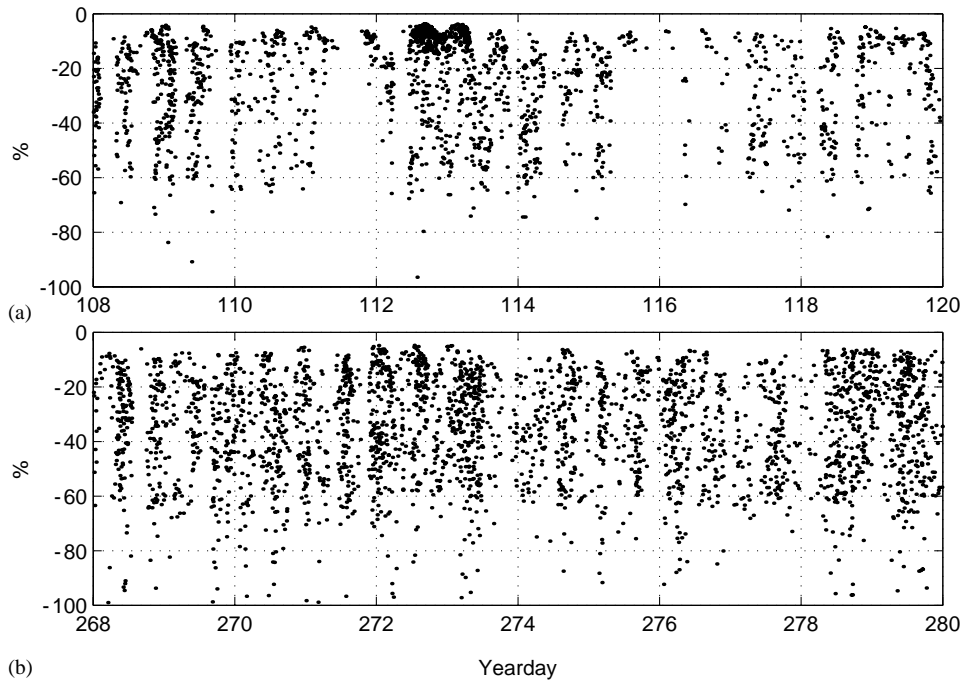


Fig. 16. Percentage change in current speed exhibited by spikes in spiked records: (a) PROCS 99-1: mean =  $-26.6\%$ , standard deviation =  $20.9\%$  and (b) PROCS 99-3: mean =  $-40\%$ , standard deviation =  $30.1\%$ .

moorings as indicated by the tilt meters. On Georges Bank, the *continuous* underreading increased in magnitude with speed as the frequency of mooring vibration, and so that of the perturbation of the instruments increased with the Strouhal frequency,  $\sigma_{\text{strouhal}} = u/5d$ , where  $u$  is the current speed and  $d$  is the diameter of the submerged obstruction.

Our data show *isolated* drops in current speed however, as opposed to a continuous underreading, but as our instruments sampled at a higher rate than usual (once per minute compared to once per 5 or 30 min) we consider the possibility that individual spikes may be smoothed out during the vector-averaging process resulting in an inaccurately low speed. The despiked data, resampled at 5 min intervals, is thus plotted against the 5-min vector-averaged current speed for the spiked records (Fig. 17), from which it can be seen that there is no increase in underreading with current speed in the vector-averaged time series as compared to the cleaned data. If we further take

into account the current direction as described in Section 3.4, we reject instrumental causes alone for the spikes for the following reasons:

- The frequency of vortex-shedding driving mooring vibration, and thus the extent of underreading, increases with current speed; there is no evidence to suggest that the frequency, or density, of spikes in our data increases with speed.
- The predominantly clockwise deflections associated with the spikes is not consistent with the negligible scatter associated with the rotor shielding mechanism, nor with the equal scatter in both directions that would be attributed to a simple mooring line vibration.
- Mooring vibration as a mechanism facilitating underreading is omnidirectional, whereas our results show the spikes to be dependent on the current direction, occurring only within a range of headings corresponding to a positive long-slope flow.

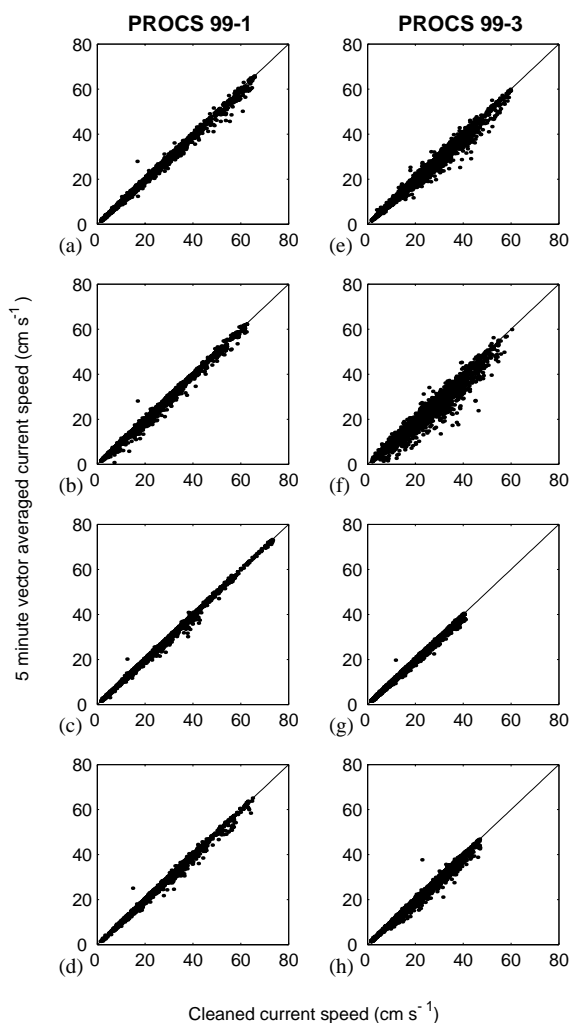


Fig. 17. Cleaned current speed (cf. Section 4) against 5-min vector-averaged current speed for all spiked records. PROCS 99-1:  $a = 700$  m,  $z = 34$  m;  $b = 700$  m,  $z = 21$  m;  $c = 777$  m,  $z = 47$  m;  $d = 1000$  m,  $z = 34$  m. PROCS 99-3:  $e = 550$  m,  $z = 47$  m;  $f = 550$  m,  $z = 34$  m;  $g = 800$  m,  $z = 47$  m;  $h = 1000$  m,  $z = 47$  m.

#### 4.3. Physical processes near the seabed

Having rejected instrumental error alone as the cause of the spikes observed in our data, we consider forcing mechanisms originating from the physical environment. We first assume that the negative bias represented by the spikes is due to the cosine response of the RCM-8 when

misaligned with the mean flow, in this case caused by rapid perturbations with a period of less than a minute so that the signal is aliased. We base this assumption on the observation that the accelerations measured by the RCM-9s, whilst enhanced during periods when the RCM-8s were subject to spikes (Fig. 8b), show no preference to a negative or a positive acceleration (Fig. 8a). This implies that the negative bias in the RCM-8 records is due to the inadequacy of the instruments' mechanical sampling strategy in resolving highly energetic motions with durations less than the sampling period, whilst the higher spatial and temporal averaging by the RCM-9s results in a more random, noisy record during turbulent periods. The high-frequency variance in the tilt meter data (Fig. 9c) further suggests short period perturbations to be present at  $z = 30$  m. We emphasise that this does not represent an instrumental error, as the forcing mechanism for the error is a genuine physical process, the signal of which, however, is aliased. We identify three mechanisms that are consistent with our observations, relating to the generation of turbulence in the BBL and its intermittent appearance at heights above the seabed greater than that would be expected for a frictional boundary layer over a flat bottom.

##### 4.3.1. Instability in the bottom Ekman layer

Trowbridge and Lentz (1991) and Lentz and Trowbridge (1991) demonstrated both theoretically and observationally how stratification, planetary rotation and a sloping bottom combine to produce an asymmetric response in the BBL during upwelling and downwelling flows. During poleward flows (with shallow water to the right in the northern hemisphere) a downwelling Ekman transport advects light water downslope, reducing the density difference between the boundary layer and the interior, and enhancing vertical turbulent transport and the growth of the BBL. In contrast, equatorward flows favour upwelling conditions, where Ekman transport advects dense water upslope, enhancing the stratification and suppressing turbulent transport. The Ekman veering (anticlockwise towards the bottom) is greatest at the top of the BBL where the density difference is greatest (Weatherly and Martin, 1978).

Our results are consistent with the above mechanism as a means of facilitating the turbulence that causes the spikes in our observations. We clearly see the spikes to occur when the hourly averaged current is poleward and aligned along the slope (Fig. 10), and when the veering is anticlockwise towards the bottom in the correct sense for a downslope Ekman transport (Fig. 18). As the BBL thickens due to turbulent mixing, the height where the maximum veering occurs increases. The increase with time in veering,  $\Delta D_0$  (observed difference in direction between  $z = 8$  and  $47$  m), during downwelling phases, often reaching  $90^\circ$  towards the end of the spiked periods, suggests  $d_0$  as nearing that of the uppermost RCM at  $z = 47$  m. This is consistent with observations from CTD casts suggesting  $d_0$  as approaching

50 m (Fig. 13). Furthermore, spikes are absent during phases favourable for upwelling when the mean current is equatorward.

The increase in veering with time may be related to the varying boundary-layer thicknesses associated with the anticlockwise and clockwise current components,  $d_+$  and  $d_-$ , respectively, of an oscillating planetary flow (Soulsby, 1983):

$$d_{\pm} = \frac{Cu_{*m}}{\sigma \pm f}, \quad (8)$$

where  $C$  is a constant,  $u_{*m}$  is a friction velocity and  $\sigma$  is the frequency of the oscillation (i.e. the tidal frequency). The consequence of (8) is that the actual BBL is composed of two counter rotating boundary layers superimposed on each other, with the anticlockwise component having a smaller

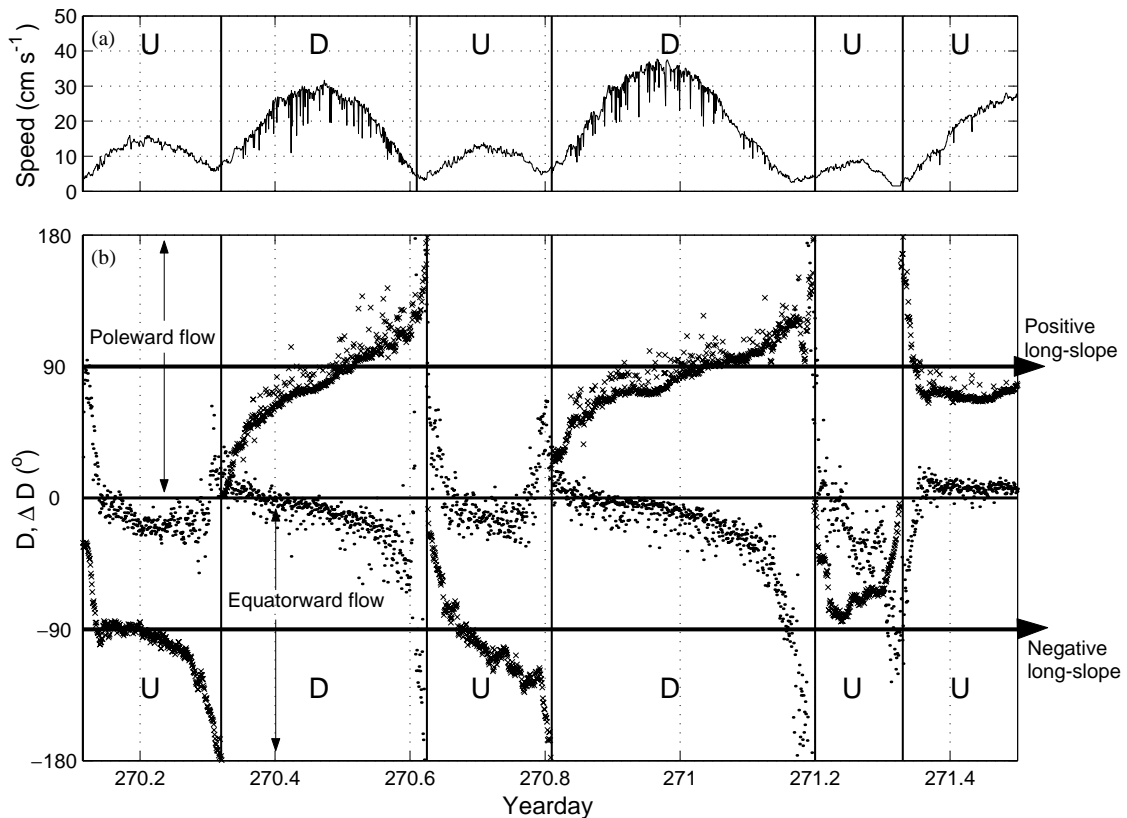


Fig. 18. (a) Speed and (b) direction,  $D$  (crosses), from  $z = 47$  m at 800 m, PROCS 99-3, and difference in direction,  $\Delta D = D_{47} - D_8$  (dots), between  $z = 47$  and 8 m. Negative values for  $\Delta D$  represent anticlockwise rotation towards the bottom, consistent with Ekman downslope transport during poleward flows. U = upwelling favourable phase, D = downwelling favourable phase.

vertical extent than the clockwise. Thus, as time passes, the clockwise component of the BBL grows, whilst the anticlockwise component remains constricted near the bottom, with the result that an apparent increase in veering in the clockwise sense upwards takes place.

#### 4.3.2. Turbulent bursting

The intermittency of the spikes may be explained by the bursting phenomenon from turbulent boundary layers (Kline et al., 1967; Gordon, 1974; Heathershaw, 1974; Gordon and Witting, 1977; Blackwelder and Haritonidis, 1983; Heathershaw and Thorne, 1985; Luchik and Tiederman, 1987; Komori et al., 1989). Turbulence is generated in the boundary region and ejected into the interior with a quasi-periodicity in the form of bursts of low momentum fluid, which are purportedly the dominant contributors to the Reynolds stress in the BBL. A burst begins as a streak of low speed fluid near the wall, which then begins to oscillate and lift away from the wall before the streak filament is ejected away from the boundary in a coherent manner (Luchik and Tiederman, 1987). Our spikes represent, in general, single data points of 1 min, implying their forcing to have a duration of less than 1 min. The duration of bursts was found by both Heathershaw (1974) and Gordon (1974), in the Irish Sea and the Choptank River estuary, respectively, to be  $\sim 10$  s, and whilst laboratory experiments are of limited applicability to the geophysical scale inherent to our present work, it is clear that the duration of bursts is most likely less than 1 min.

The random, intermittent nature of bursting is accepted as an inherent property of the turbulence, but the coherent structure of the bursts themselves has prompted efforts to define a mean period,  $T_B$ , between their occurrence. Questions exist over whether to scale  $T_B$  with variables characteristic of the inner wall region, ( $u_\tau$ ,  $\nu$ ), the friction velocity and the kinematic viscosity, or variables characteristic of the outer region, ( $U_\infty$ ,  $d$ ), the free stream velocity and the boundary layer thickness. Whilst some laboratory experiments suggest the inner variables to be applicable to scaling, more recent work tends towards either a mix of the inner and outer variables (Kumar et al., 1998) or either inner

variables or outer-flow variables and the Reynolds number,  $Re$  (Komori et al., 1989). We choose to scale with the outer variables for two reasons: firstly, scaling with the inner variables requires knowledge of the Reynolds stresses to calculate the friction velocity. Our measurements prohibit us from measuring the Reynolds stresses and thus the uncertainty introduced by estimating the friction velocity could create an error comparable to that associated with scaling using the outer variables. Secondly, recent work suggests that the need to scale with inner variables may simply be a consequence of the differences in  $Re$  between laboratory experiments, where  $Re \approx O(10^3)$ , and the geophysical environment, where typically  $Re > O(10^6)$  (Nimmo Smith et al., 1999). Scaling with ( $U_\infty$ ,  $d$ ) (Rao et al., 1971; Laufer and Badri Narayanan, 1971)

$$T_B = 5 \left( \frac{d}{U_\infty} \right), \quad (9)$$

where  $8 < d < 100$  m is the approximate height of the BBL as defined by (6), and taking  $U_\infty = 40 \text{ cm s}^{-1}$ , we find  $100 < T_B < 1025$  s. CTD casts indicate  $d > 20$  m (Fig. 13), and at times exceeding 50 m for which  $T_B = 625$  s. This is consistent with the quasi-period of the spikes in the spiked records, calculated as the time between spikes after discounting gaps in excess of 30 min. We find  $T_{B \text{ minimum}}$  of 313 s at  $z = 34$  and 550 m during PROCS 99-3, and  $T_{B \text{ maximum}}$  of 552 s at  $z = 34$  and 1000 m during PROCS 99-1.  $T_B$  for all the spiked records is 465 s. The thickening of the boundary layer and the subsequent ejection of turbulent fluid upwards furthermore explains the trend for spikes to appear higher up the mooring at  $z = 34$  and 47 m (cf. Section 3.2). As explained above, we expect to find the maximum Ekman veering at the upper limit of the BBL, and we tentatively propose that the clockwise deflections associated with the spikes are related to Ekman veering (clockwise from the bottom) as the fluid is ejected upwards in the form of bursts. This is not a definitive explanation, as the record from 1000 m during PROCS 99-3 exhibits a number of anticlockwise deflections which we cannot as yet explain.

A further contribution to the negative bias represented by the spikes may be due to the low momentum fluid ejected by the bursts from the near wall region. Whilst the spikes are principally due to the cosine response of the misaligned current meter, the error may be further enhanced by the lower speed of the fluid ejected as compared to the mean flow. In order to quantify the effect of the low speed fluid on the response of the RCM-8 however, a much better understanding of the structure and persistence of the bursts in a geophysical context will be required.

#### 4.3.3. Internal waves

The focus of the present research project is the interaction of internal waves with the local topography and the implications for mixing. Maximum values of  $N$  are found at 550 m where  $N \sim 45$  cpd, decreasing to  $\sim 7$  cpd at 1000 m (Fig. 6). Thus, internal waves impinging on the slope cannot be the *direct* cause of the spikes which are observed for  $\sigma > 120$  cpd. Internal waves may, however, promote conditions that facilitate the instrumental response we observe in our data by propagating *obliquely* against a sloping boundary, generating along-slope currents through the flux of incident wave momentum when the waves break (Slinn, 1999; Thorpe, 1999). The waves dissipate energy on reflection, and after a short time the mean boundary currents interact with the incoming wave field, leading to the establishment of a new turbulent boundary layer at the upper interface of the shear layer. The flux of wave momentum into the water thus occurs further from the wall, with a thicker boundary resulting later, and with the waves being no longer able to penetrate the slope (Slinn, 1999; Zikanov and Slinn, 2001). This mechanism has potential for generating turbulence higher up the moorings as observed, especially at depths  $\sim 600$  m where the stratification is sufficiently strong to support a broad internal wave band due to the influence of the permanent pycnocline. We propose, however, that the Ekman transport explained above is the dominant mechanism for generating turbulence within the BBL. Future analysis will focus on a better understanding of the role internal waves play.

## 5. Conclusions

Our data, acquired from deep-sea moorings deployed near the seabed over a sloping bottom, indicate spike-like reductions in current speed with associated deflections in current direction. The spikes and deflections occurred intermittently throughout a number of records, with quasi-periods between  $\sim 350$  and 550 s, and with a duration of less than the sampling period of 1 min, during periods when the mean flow had a predominantly positive long-slope component. We reject instrumental deficiency as the cause of the spikes, and propose turbulence generated in the BBL by downslope Ekman transport to be responsible.

The current meters are subject to a high-frequency perturbation that leads to a misalignment with the mean flow and a reduction in the observed current speed because of the cosine response of the mechanical current meters, with the low speed of the ejected fluid possibly contributing further to the negative bias. The misalignment is due to turbulence generated by the unstable stratification that results from downslope Ekman transport. The observed veering in current direction between  $z = 8$  and 47 m is in the correct sense for Ekman dynamics in the BBL of an oscillating planetary flow. This mechanism causes a thickening of the BBL, explaining why we observe most spikes at  $z = 34$  and 47 m, and is consistent with observed  $\sigma_\theta$  profiles which indicate a boundary layer of thickness comparable to that predicted by theory for sloping bottoms. During upwelling-favourable periods, when the long-slope component of the mean flow is negative, we do not see spikes, as the upslope transport of lighter water enhances the stratification, reduces the height of the BBL and suppresses vertical turbulent transport.

The intermittency of the spikes is due to the bursting phenomenon from BBL. Our results indicate both a quasi-period and a duration comparable to laboratory experiments and previous fieldwork. Ekman veering of the ejected fluid may explain the predominantly clockwise orientation of the deflections associated with the spikes, but we can as yet offer no concrete explanation for

this observation. It is hoped that future research with the direct intention of measuring this phenomenon and employing suitable instrumentation, such as the newly developed NIOZ fast response thermistor string (van Haren et al., 2001), will clarify the spatial and temporal scales of the process.

The spikes in our current speed records have implications for the reliability of rotor- and vane-type current meters in a region subject to turbulent fluctuations. An instrument sampling at a lower frequency would average out such features, and whilst we show that no apparent underreading occurs if the data are vector-averaged over 5-min intervals and compared to the cleaned data which removes the influence of the spikes, we are not sure as to the effect of the mechanism on the quality of the data at higher current speeds. The data have nonetheless provided unexpected and useful insight into the near-bed dynamics and the potential role of the BBL in mixing processes.

## Acknowledgements

The data were acquired during the Processes on the Continental Slope (PROCS) project, funded by the Netherlands Organisation for the Advancement of Scientific Research (NWO). We thank the Department of Sea Technology for preparing the moorings, and the crew of the R.V. *Pelagia* for their assistance during their deployment and recovery. We further thank Theo Hillebrand for preparing the instrumentation. This is NIOZ contribution number 3727.

## References

- Blackwelder, R.F., Haritonidis, J.H., 1983. Scaling of the bursting frequency in turbulent boundary layers. *Journal of Fluid Mechanics* 132, 87–103.
- Fofonoff, N.P., Ercan, Y., 1967. Response characteristics of a Savonius rotor current meter. Technical Report WHOI-67-33. Woods Hole Oceanographic Institution, Woods Hole, MA, 46pp.
- Garrett, C., MacCready, P., Rhines, P., 1993. Boundary mixing and arrested Ekman layers: rotating stratified flow near a sloping boundary. *Annual Review of Fluid Mechanics* 25, 291–323.
- Gordon, C.M., 1974. Intermittent momentum transport in a geophysical boundary layer. *Nature* 248, 392–394.
- Gordon, C.M., Witting, J., 1977. Turbulent structure in a benthic boundary layer. In: Nihoul, J.C.J. (Ed.), *Bottom Turbulence*, Vol. 19. Elsevier Oceanography Series, Amsterdam, pp. 59–81.
- Hamilton, J.M., Fowler, G.A., Belliveau, D.J., 1997. Mooring vibration as a source of current meter error and its correction. *Journal of Atmospheric and Oceanic Technology* 14, 644–655.
- Heathershaw, A.D., 1974. Bursting phenomena in the sea. *Nature* 248, 394–395.
- Heathershaw, A.D., Thorne, P.D., 1985. Sea-bed noises reveal role of turbulent bursting phenomenon in sediment transport by tidal currents. *Nature* 316, 339–342.
- Kalvaitis, A.N., 1974. Effects of vertical motion on vector-averaging (Savonius rotor) and electromagnetic type current meters. Technical Memo, NOAA-TM-NOS-NOIC-3, 40pp.
- Karweit, M., 1974. Response of a Savonius rotor to unsteady flow. *Journal of Marine Research* 32, 359–364.
- Kline, S.J., Reynolds, W.C., Schraub, F.A., Runstadler, P.W., 1967. The structure of turbulent boundary layer. *Journal of Fluid Mechanics* 30, 741.
- Komori, S., Murakami, Y., Ueda, H., 1989. The relationship between surface-renewal and bursting motions in an open-channel flow. *Journal of Fluid Mechanics* 203, 103–123.
- Kumar, S., Gupta, R., Banerjee, S., 1998. An experimental investigation of the characteristics of free-surface turbulence in channel flow. *Physics of Fluids* 10 (2), 437–456.
- Laufer, J., Badri Narayanan, M.A., 1971. Mean period of the turbulent production mechanism in a boundary layer. *Physics of Fluids* 14, 182–183.
- Lentz, S.J., Trowbridge, J.H., 1991. The bottom boundary layer over the North California Shelf. *Journal of Physical Oceanography* 21, 1186–1201.
- Loder, J.W., Hamilton, J.M., 1991. Degradation of some mechanical current meter measurements by high-frequency mooring or wave-motion. *IEEE Journal of Oceanic Engineering* 16 (4), 343–349.
- Loder, J.W., Pettipas, R.J., Belliveau, D.J., 1990. Intercomparison of current measurements from the Georges Bank Frontal Study. Canadian Technical Report of Hydrography and Ocean Sciences, No. 127.
- Luchik, T.S., Tiederman, W.G., 1987. Timescale of ejections and bursts in turbulent channel flows. *Journal of Fluid Mechanics* 174, 529–552.
- MacCready, P., Rhines, P.B., 1993. Slippery bottom boundary layers on a slope. *Journal of Physical Oceanography* 23, 5–22.
- Nimmo Smith, W.A.M., Thorpe, S.A., Graham, A., 1999. Surface effects of bottom-generated turbulence in a shallow tidal sea. *Nature* 400, 251–253.
- Rao, K.M., Narashima, R., Badri Narayanan, M.A., 1971. The “bursting” phenomenon in a turbulent boundary layer. *Journal of Fluid Mechanics* 48, 339–352.

- Saunders, P.M., 1976. Near-surface current measurements. *Deep-Sea Research I* 23, 249–258.
- Saunders, P.M., 1980. Overspeeding of a Savonius rotor. *Deep-Sea Research I* 27A, 755–759.
- Slinn, D.N., 1999. Along-slope current generation by obliquely incident internal waves. 'Aha Huliko' a Proceedings, Hawaiian Winter Workshop, SOEST Special Publication, 1999, pp. 141–147.
- Soulsby, R.L., 1983. The bottom boundary layer of shelf seas. In: Johns, B. (Ed.), *Physical Oceanography of Coastal and Shelf Seas*, Vol. 35. Elsevier Oceanography Series, Amsterdam, pp. 189–266.
- Thorpe, S.A., 1999. The generation of alongslope currents by breaking internal waves. *Journal of Physical Oceanography* 29, 29–38.
- Trowbridge, J.H., Lentz, S.J., 1991. Asymmetric behaviour of an oceanic boundary layer above a sloping bottom. *Journal of Physical Oceanography* 21, 1171–1185.
- van Haren, H., 1996. Correcting false thermistor string data. *Continental Shelf Research* 16 (14), 1871–1883.
- van Haren, H., Groenewegen, R., Laan, M., Koster, B., 2001. A fast and accurate thermistor string. *Journal of Atmospheric and Oceanic Technology* 18, 256–265.
- Weatherly, G.L., Martin, P.J., 1978. On the structure and dynamics of the oceanic bottom boundary layer. *Journal of Physical Oceanography* 8, 557–570.
- Zikanov, O., Slinn, D.J., 2001. Along-slope current generation by obliquely incident internal waves. *Journal of Fluid Mechanics* 445, 235–261.